Determining the Elasticity of Materials Employing Quantum-mechanical Approaches: From the Electronic Ground State to the Limits of Materials Stability

M. Friák[1)*], T. Hickel[1)], F. Körmann[1)], A. Udyansky[1)], A. Dick[1)], J. von Pezold[1)], D. Ma[1)], O. Kim[1)], W.A. Counts[1)], M. Šob[2,3)], T. Gebhardt[4)], D. Music[4)], J. Schneider[4)], D. Raabe[1)], and J. Neugebauer[1)]

[1)] Max-Planck-Institut für Eisenforschung GmbH, Max-Planck-Strasse 1, D-40237, Düsseldorf, Germany
[2)] Department of Chemistry, Faculty of Science, Masaryk University, Kotlářská 2, 61137 Brno, Czech Republic
[3)] Institute of Physics of Materials, Academy of Sciences of the Czech Republic, Žižkova 22, 61662 Brno, Czech Republic
[4)] Materials Chemistry, RWTH Aachen University, D-52056 Aachen, Germany
* Corresponding author; e-mail: m.friak@mpie.de

Quantum-mechanical (so-called *ab initio*) calculations have achieved considerable reliability in predicting physical and chemical properties and phenomena. Due to their reliability they are becoming increasingly useful when designing new alloys or revealing the origin of phenomena in existing materials, also because these calculations are able to accurately predict basic material properties without experimental input. Due to the universal validity of fundamental quantum mechanics, not only ground-state properties, but also materials responses to external parameters can reliably be determined. The focus of the present paper is on *ab initio* approaches to the elasticity of materials. First, the methodology to determine single-crystalline elastic constants and polycrystalline moduli of ordered compounds as well as disordered alloys is introduced. In a second part, the methodology is applied on α-Fe, with a main focus on (i) investigating the influence of magnetism on its elasticity and phase stability and (ii) simulating extreme loading conditions that go up to the theoretical tensile strength limits and beyond.

Keywords: ab initio, elasticity, magnetism, stability, strength

Submitted on 10 November 2010, accepted on 19 November 2010

Introduction

Most materials properties can be traced back to the behaviour of electrons that hold atoms together. An important strategy of condensed matter theory is, therefore, to calculate the electronic structure (ES) of solids, in order to determine their physical and chemical properties. More specifically, the laws of quantum mechanics and electrodynamics as expressed in the Schrödinger equation are used to describe the interaction of electrons and atomic cores precisely and without any experimental input parameters. Such simulations, starting from identical principles and building blocks, are called first principles methods or, using the corresponding Latin term, *ab initio* methods.

A general solution of the quantum mechanical equations for ES including all known interactions between the electrons and atomic nuclei in solids is computationally very demanding. That is why practical ES calculations in solids were rather rare prior to the availability of large high-speed computers. Even with increasing computational resources, a series of approximations must be employed in order to make a comprehensive solution for most non-trivial systems feasible. In many cases, however, it is nowadays possible not only to simulate certain experimental conditions and set-ups with high accuracy, but also to design new materials and to predict their properties before actually casting them. The success of such a *computational materials science* is to a large extent related to the development of density functional theory (DFT) [1, 2], which was awarded a Nobel Prize in Chemistry in 1998 (Prof. W. Kohn). In case of DFT calculations, highly precise solutions of the one-electron Kohn-Sham equation for a solid are determined and provide an understanding of matter at the atomic and electronic scale with an unprecedented level of detail and accuracy.

Importantly, *ab initio* calculations can also provide data on the atomic scale that are inaccessible experimentally. For example, the value of theoretical strength, as the upper limit of attainable stresses in a material, is rather challenging to measure due to the fact that most samples contain internal defects leading to material's failure well below its theoretical strength. As an indirect consequence, such a lack of experimental data for far-from-equilibrium states leads to a limited applicability of semiempirical computational approaches that are fitted to measured data. In contrast, *ab initio* calculations are reliable for heavily strained conditions equally well as for the ground state, due to the universal validity of the laws of quantum mechanics.

As a modern trend in materials science, results of quantum-mechanical calculations have been combined with other methods within various multi-disciplinary schemes what significantly broadens their use well beyond the atomistic level (for a combination with FEM simulations see e.g. [3, 4]). In such multi-scale modelling of materials or scale-hopping approaches, the role of *ab initio* calculations is mostly two-fold: (i) to study the cases where the electronic effects are crucial and must be treated from first principles and (ii) to provide data for the generation of inter-atomic

potentials with an extended range of transferability (see e.g. [5]). Let us note that there exists a vast amount of literature devoted to multiscale modelling of materials (recent reviews may be found for example in [6–9]).

In this paper we focus on the determination of elastic parameters of materials based on *ab initio* methods and including approaches to single-crystalline elastic constants and polycrystalline moduli of pure elements, ordered compounds, as well as disordered alloys. In the case of bcc ferromagnetic iron, the role of magnetism and different magnetic states on its elasticity is analyzed and it is shown that the magnetic state of iron and its elastic properties are closely related to (i) the thermodynamic stability of α-Fe, (ii) its phase transformations as well as (iii) its response to extreme loading conditions including uniaxial tensile loading and isotropic triaxial loading.

Elastic Constants Calculations

The elastic behavior of a completely asymmetric material is specified by 21 independent elastic constants. In case of systems possessing a cubic symmetry (such as e.g. α-Fe), however, only three elastic constants C_{11}, C_{12}, and C_{44}, must be determined from simulations of three independent straining modes. When straining the lattice, the corresponding changes of the total energy as a function of the applied strain are calculated employing *ab initio* methods. A straight-forward distortion is the isotropic volume change, which allows the determination of the bulk modulus B_0 from the fitting of the calculated energy-volume dependence to an equation of state. Other commonly used distortions are tetragonal and trigonal ones (for details see e.g. Chen et al. [10] and Söderlind et al. [11]).

These three types of lattice strain (see **Fig. 1**) lead to total-energy dependences which can be fitted to (i) an equation of state (as, e.g., Murnaghan's [12]) and to (ii) quadratic functions in case of the volumetric changes and tetragonal/trigonal strains, respectively. Employing the fitting, the bulk modulus B_0 and the three single crystal elastic constants can be calculated:

$$B_0 = V\frac{\partial^2 E}{\partial V^2} = \frac{(C_{11}+2C_{12})}{3}, \quad \frac{\partial^2 U^{tet}}{\partial \delta^2} = \frac{3}{2}(C_{11}-C_{12}), \frac{\partial^2 U^{tri}}{\partial \delta^2} = 4C_{44}. \tag{1}$$

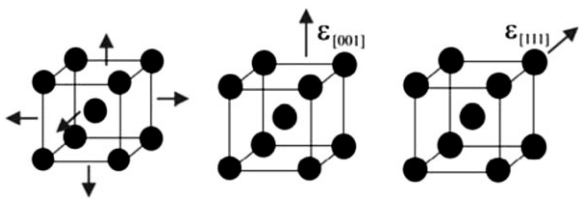

Figure 1. Schematic visualization of three independent loading modes (volumetric changes, tetragonal and trigonal strains, respectively) applied to a body-centered cubic system in order to determine the C_{11}, C_{12}, and C_{44} elastic constants.

Here δ is the strain (or distortion), E is the total energy, V the volume, U^{tet} is the strain energy density due to the tetragonal strain, and U^{tri} is the strain energy density due to the trigonal strain.

The character of the total energy dependence on the strain can be directly used to identify unstable phases: The total energy E has a minimum for the unloaded ground state and forms a convex curve for mechanically stable systems ($dE > 0$) for all possible loading types. For mechanically unstable states the total energy for at least one loading mode has a concave character with the maximum for the unloaded state ($dE < 0$).

Having the single-crystalline elastic constants C_{ij}, or elastic compliances S_{ij}, estimates of polycrystalline moduli can be derived using various homogenization schemes. The upper (or Voigt [13]) bound and the lower (or Reuss [14]) bound of the polycrystalline modulus values are the following:

$$B_R = B_V = B_0, G_R = \frac{5}{4(S_{11}-S_{12})+3S_{44}}, \quad G_V = \frac{C_{11}-C_{12}+3C_{44}}{5}. \tag{2}$$

Here, B_R and B_V are the Reuss and Voigt bounds of bulk modulus and G_R and G_V are the Reuss and Voigt bounds of shear modulus. Additionally, the polycrystalline shear modulus can be estimated using a self-consistent approach, which usually provide results better than either Voigt or Reuss solutions. The self-consistent approach derived by Hershey [15] for texture-free aggregates with cubic symmetry, simplifies to the following equation:

$$\begin{aligned} &64G_H^4 + 16(4C_{11}+5C_{12})G_H^3 \\ &\quad + \left[3(C_{11}+2C_{12})(5C_{11}+4C_{12}) - 8(7C_{11}-4C_{12})C_{44}\right] \\ &\quad \cdot G_H^2 - (29C_{11}-20C_{12})(C_{11}+2C_{12}) \\ &\quad \times C_{44}G_H - 3(C_{11}+2C_{12})^2(C_{11}-C_{12})C_{44} = 0. \end{aligned} \tag{3}$$

Once the homogenized values of G and B are known, then the Young's modulus (Y) of an elastically isotropic polycrystalline aggregate can be calculated:

$$Y = \frac{9B_0G}{3B_0+G}. \tag{4}$$

Here G denotes either G_V, G_R, or G_H. In this way, for each pure element or ordered compound with cubic symmetry, the complete set of elastic constants can be determined (see, e.g., [16–25]).

Compositional dependences of both elastic constants and polycrystalline moduli can be obtained applying the above mentioned methods for supercells with different constituent concentrations. In this way elastic constants of chemically ordered phases can nowadays be routinely calculated (at least at $T = 0\,K$) using electronic structure methods. The prediction of the elastic properties of low-symmetry systems, such as random alloys is, however, less

straightforward. In particular, the faithful reproduction of randomness in these structures poses a significant challenge. A *naïve* atomistic description of random alloys based on a statistical distribution of atoms requires a considerable configurational space and hence can only be achieved using large supercells, which renders standard electronic structure methods unfeasible. Instead, three alternative approximations are generally employed to mimic the disorder: the coherent potential approximation (CPA), the concept of special quasi-random structures (SQSs), and, to obtain the temperature dependencies of material properties including configurational entropy, the cluster expansion (CE) approach turns out to be a valuable tool [26].

The CPA describes the random distribution of impurity atoms (within a mean-field framework) by a concentration-dependent effective potential which averages the scattering properties of the ordered alloy constituents and reproduces the electronic properties of the actual alloy when placed on every matrix site [27]. In SQS randomness is introduced by mimicking as closely as possible the most relevant nearest neighbour pair and multisite correlation functions of an infinite random alloy within a finite supercell [28] (an example of SQS supercell is shown in **Fig. 2**).

In most cases, both approaches provide similar results, as for instance demonstrated for the Mo-Nb system (**Fig. 3**). Here, the CPA calculations have been performed within the exact muffin-tin approximation (EMTO) [31], while the SQS implementation via the correlation functions is obtained with the alloy theoretical automated toolkit (ATAT) [32, 33], which was used together with Vienna *ab initio* software package (VASP) [34, 35]. More details on these calculations can be found elsewhere [36, 37]. The bulk modulus calculated with both CPA and SQS approaches increases with increasing the Mo concentration x in Mo_xNb_{1-x} solid solution with an almost identical slope. The comparison with experiment [30] demonstrates the good performance of both CPA and SQS methods. The SQS usually yields better results for alloys with atomic size mismatch, in which relaxation effects may be significant.

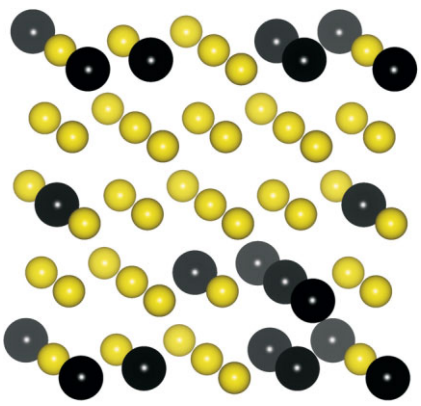

Figure 2. Example of a fcc-based 32-atomic special quasi-random structure $A_{25}B_{75}$ containing eight 4-atomic elementary fcc cells with the A atoms visualized as dark larger spheres and B atoms as yellow smaller spheres [29].

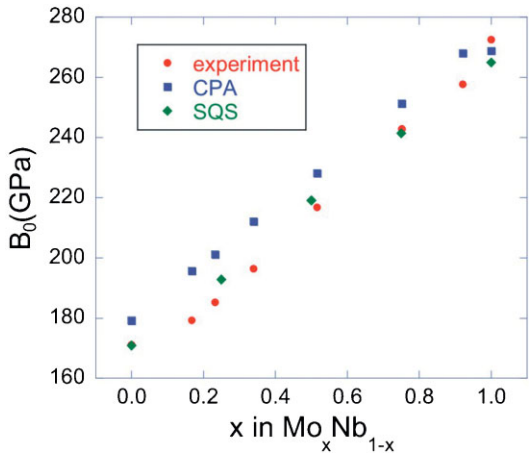

Figure 3. Bulk modulus (B_0) of Mo_xNb_{1-x} as a function of alloy composition x. Theoretical results obtained employing coherent phase approximation (CPA) and special quasi-random structures (SQS) are compared with experimental data [30].

The CPA works well for coherent alloys consisting of chemical species of similar size and has the advantage that arbitrary alloy compositions are readily accessible without any additional computational cost. It can be improved to the locally self-consistent Green's function (LSGF) method [38], which allows to include even local environment effects.

Whereas Fig. 3 indicates a rather linear dependence of the bulk modulus as a function of chemical composition, this is by no means a general feature of all elastic constants and materials. In order to show an example of the non-linearity of the compositional dependence of elastic constants of alloys employing the SQS approach, the deviation of both single-crystalline elastic constants and homogenized polycrystalline moduli are shown in **Fig. 4** for the Ti-Al fcc solid solution [29]. Specifically, for a given elastic constant $C(A_xB_{1-x})$ the deviation from the linear behaviour $\Delta C(A_xB_{1-x})$ in percent is shown. The deviation is defined as the difference between (i) the actual value $C(A_xB_{1-x})$ and (ii) the value obtained from the linear interpolation $(x \cdot C(A) + (1-x) \cdot C(B))$ between the elastic constants of the elemental end-members C(A) and C(B) forming the binary system.

The visualized compositional trends of non-linear parts of both single-crystalline elastic constants C_{11}, C_{12}, C_{44} and the homogenized Young's modulus Y clearly show that the non-linear parts can amount easily up to 40–50% of the actual values and differ quantitatively when comparing different elastic constants or elastic moduli. Further, it is noteworthy that the non-linear features of the elastic constants do not average out when performing the homogenization in order to determine the polycrystalline moduli [17].

Due to the fact that the chemical trends exhibit rather strong non-linear features and may thus not be easily estimated from values tabulated for pure constituents, a series of experiments for each concentration must be performed or, alternatively, a series of quantum-mechanical

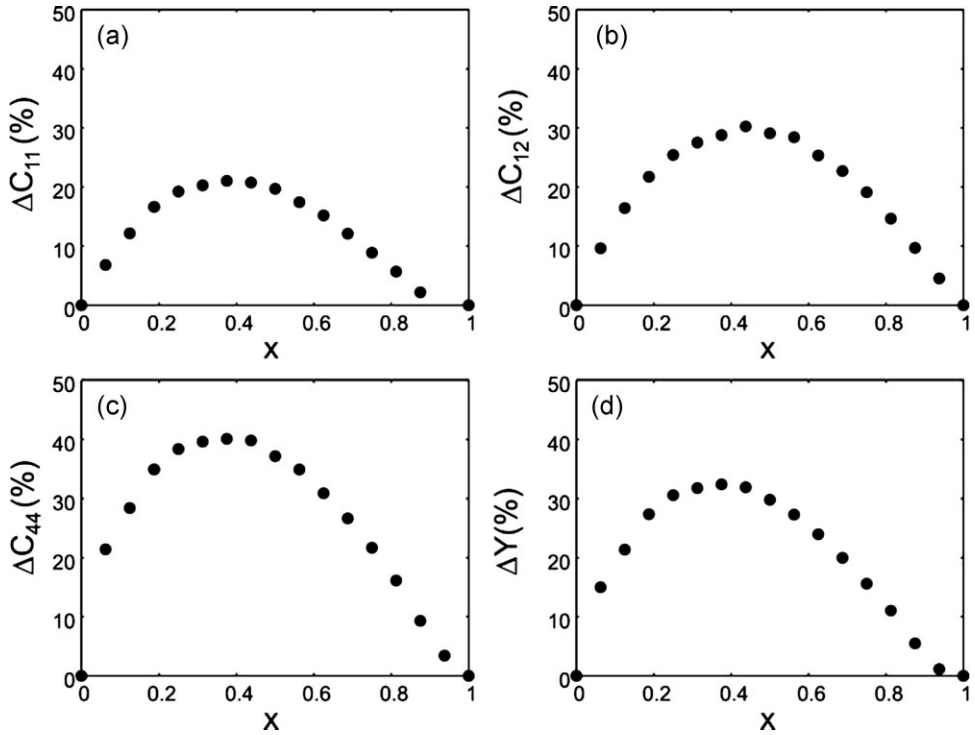

Figure 4. Compositional trends in the non-linear part of the elastic constants ΔC_{11} (a), ΔC_{12} (b), ΔC_{44} (c), and polycrystalline Young's modulus ΔY (d) homogenized employing the Voigt scheme as a function of the composition x in the Ti_xAl_{1-x} fcc-based solid solutions (for details see [29]).

calculations is needed. The latter way, or an optimum combination of both, can significantly reduce both costs and time that are necessary to identify an alloy with desired elastic properties (see the theory-guided materials design discussed in Section 5).

Results Obtained for Iron

In this paper, we mostly apply the above described methodology (and its extension to a broader range of lattice distortions) to iron that is exhibiting a variety of magnetic structures. Therefore, magnetic effects play a crucial role in the phase stability of iron and iron-based systems. Body-centered cubic (bcc) iron is ferromagnetic in its ground state with the experimentally measured local atomic magnetic moment around 2.1–2.2 μ_B (so-called high-spin state). The value and the arrangement of orientations of the local magnetic moment of neighbouring Fe atoms are essential for a variety of iron's properties, including its elasticity or phase transitions.

Structurally, iron can exist also in the face-centered cubic (fcc) γ phase (in, e.g., thin films or at elevated temperatures), in the hexagonal ε phase (under hydrostatic pressure) or in a variety of tetragonal, trigonal, or orthorombic phases (in thin films or locally at grain boundaries [39–41]). As summarized below, these phase transitions are closely related to the elasticity if the applied strains are extended beyond the harmonic regime (quadratic law) for the total energy. Within this context, certain changes of both the magnitude of the local magnetic moment and/or transitions from ferromagnetic (FM) to various antiferromagnetic states (AFM) can lead to the loss of stability and a phase transformation.

Below, we first determine the single-crystalline elastic constants and polycrystalline elastic moduli of ferromagnetic high-spin state of bcc Fe. Second, we extend the range of applied deformations to identify limits of iron stability with respect to transformations that preserve the atomic volume (tetragonal Bain's path, Stoner-like excitations, trigonal transformation, and finally the cubic-to-hexagonal one) paying special attention to differences stemming from different magnetic states. In order to examine their dependence on hydrostatic pressures these transformation paths are studied not only at the equilibrium volume of bcc FM Fe, but also at different volumes. Finally, we determine the behaviour of iron under loading conditions that allows for structural relaxations including volumetric changes, specifically Poisson's contraction during the tensile test along the [001] and [111] directions, as well as triaxial loads.

Elastic constants of α-Fe. Unless explicitly specified, the following results were obtained within density-functional theory [1, 2] employing the generalized gradient approximation [42] as implemented in the Wien97 code [43]. Employing the above described methodology, the calculated elastic constants and the homogenized polycrystalline modulus of ferromagnetic bcc Fe are summarized in **Tab. 1**.

As can be seen from the comparison of theoretical and experimental values given in Tab. 1, the agreement between predicted *ab initio* and measured elastic parameters is within

Table 1. Theoretically predicted and experimental [44] single-crystalline elastic constants C_{11}, C_{12}, and C_{44} together with poly-crystalline shear and Young's moduli of α-Fe, G and Y, respectively.

	C_{11}	C_{12}	C_{44}	G	Y
Theory	250	124	99	82.4	212
Exp. [34]	242	147	112	80.2	209

∼10%. The deviations stem mostly from approximations in the exchange-correlation functional. For a detailed analysis of how such errors affect homogenized elastic properties, error propagation of different homogenization schemes has been analyzed in Ref. [17].

Stability along tetragonal transformation path. After analyzing ground-state elasticity of Fe, the small lattice strains, which have been applied in order to determine the values of single-crystalline elastic constants, can be extended in order to identify limits of stability of the ferromagnetic state of iron. To analyze the competition between different magnetic states in different tetragonal structures (see, e.g., [45–51]), the range of the tetragonal lattice distortions associated with the $C' = ½ (C_{11} - C_{12})$ elastic constant (see Fig. 1 and Eq. (1)) is extended to follow the so-called Bain's transformation path connecting the bcc and fcc structures via a martensitic transformation (**Fig. 5**).

Along the Bain's path, the symmetry of the structures is reduced to the tetragonal one, but the bcc and fcc structures represent phases of higher symmetry along the path. When studying the behaviour of the total energy along the deformation paths, one usually assumes that the atomic volume is constant. The Bain's path can be then conveniently described by the ratio c/a of tetragonal-lattice parameters (see Fig. 5), with $c/a = 1$ for the bcc phase and $c/a = \sqrt{2}$ for the fcc structure. For magnetic materials that are considered in this section it is important to note that certain arrangements of the magnetic moments can reduce the symmetry even further (see **Fig. 6**).

The total-energy changes along the Bain's path have been calculated and are visualized as a function of the path parameter c/a for each magnetic state in **Fig. 7**. The character of the total-energy dependences significantly differs for

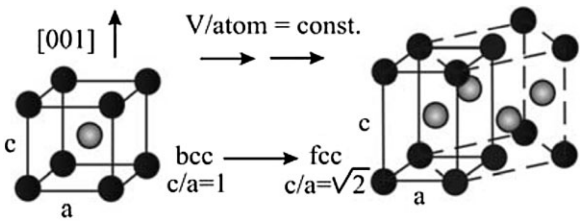

Figure 5. Schematic visualization of Bain's transformation path transforming the bcc phase into the fcc one or vice versa. The labels "c" and "a" indicate the length scales along the $[001]_{bcc}$ and $[100]_{bcc}$ directions, respectively. The body-centered atom in the bcc cell is indicated by a semi-filled circle to identify its position after the transformation in the fcc cell.

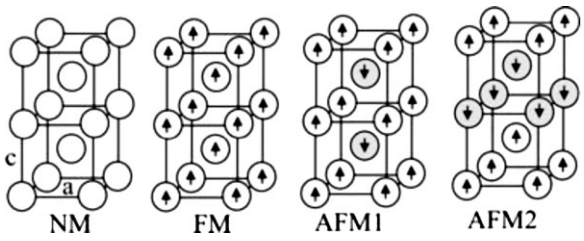

Figure 6. Schematic pictures of three selected magnetic states of iron including the non-magnetic (NM) state, ferromagnetic (FM) one, and two anti-ferromagnetic states (AFM1 and AFM2). Different orientations of local magnetic moments are indicated by arrows.

different magnetic states, specifically contrasting ferromagnetic (FM) states and the other three states, the non-magnetic (NM) and the two anti-ferromagnetic states (AFM1 and AFM2). The curvatures of the total-energy dependencies for the bcc structure determine the value of C' elastic constants of each individual magnetic state. The corresponding magnetic moment (2.25 μ_B) is very close to the experimentally detected values 2.1 – 2.2 μ_B.

Craievich and co-workers [52] have shown that some energy extrema on constant-volume transformation paths are dictated by symmetry. Namely, most of the structures encountered along the transformation paths between some higher-symmetry structures, for instance between bcc and fcc at the Bain's path, have a symmetry that is lower than cubic. At those points of the transformation path where the symmetry of the structure is higher, the derivative of the total energy with respect to the parameter describing the path must be zero. These are so-called symmetry-dictated extrema. The extrema are clearly seen in Fig. 7 in case of FM bcc Fe (minimum), NM and AFM1 bcc Fe (maxima), as well as for the FM and NM fcc Fe (minima). The AFM2 state does not have the cubic symmetry for neither $c/a = 1$ nor for $c/a = \sqrt{2}$, and the total energy at these points has a finite slope without any extremum.

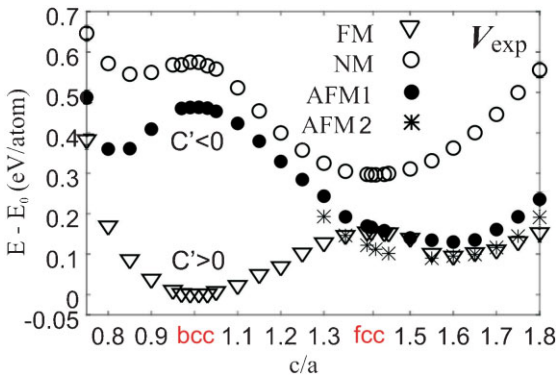

Figure 7. Calculated total energy E (with respect to the energy of the ground state E_0) along the Bain's path for the non-magnetic (NM) state, ferromagnetic (FM) state, and two anti-ferromagnetic states (AFM1 and AFM2). All results have been calculated for a constant volume equal to the experimental volume of α–Fe.

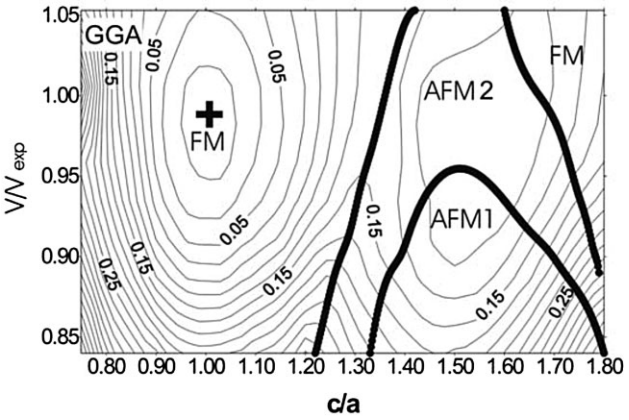

Figure 8. Calculated contour-plots of the total energy E of α–Fe (with respect to the energy of the ground state E_0) as a function of the c/a path parameter and the volume (relative with respect to the experimental volume of α–Fe). The ground-state configuration is marked by a cross. The contour lines are separating energies with a difference of 0.02 eV/atom.

However, other extrema which are not dictated by the symmetry and reflect properties of the specific material (as, e.g., the minimum of the AFM2 state) may occur. Configurations which correspond to energy minima at the transformation paths represent stable or metastable structures and may mimic atomic arrangements that could be encountered when investigating thin films (see, e.g., [45]) and extended defects such as interfaces or dislocations.

The results visualized in Fig. 7 were obtained for states with an atomic volume equal to the experimental value detected for α–Fe. Similar dependencies can be calculated also for other volumes and allow to check the stability of different phases, e.g., under hydrostatic pressure. The results are shown in **Fig. 8** for a series of nine different volumes ranging from 84% to 105% of the experimental atomic volume of bcc FM Fe. Only the energies of state with the lowest total energy (among the calculated ones) for a given c/a ratio and volume are shown.

The thick lines in Fig. 8 indicate phase boundaries, which separate regions with different magnetic states of Fe, obtained by a total energy minimization with respect to c/a ratio and atomic volume. Apart from the large region of the FM bcc phase ($c/a = 1.0$), there are AFM2 and AFM1 regions in the neighbourhood of the fcc structure ($c/a = \sqrt{2}$). Note, that the lattice symmetry of fcc iron with the AFM1 and AFM2 spin ordering is tetragonal and, therefore, we do not find any extremum of the total energy of these states (dictated by symmetry) at $c/a = \sqrt{2}$. The phase boundary between the FM and AFM2 states can be considered as a stability limit of the FM bcc Fe. Among others, the contour plot presented in Fig. 8 allowed to predict magnetic states of stable iron overlayers at (001) substrates with different lattice parameters [42].

Since the curvature of the total-energy plots shown in Fig. 7 determine the value of elastic constant C', the change of the magnetic state from the FM to AFM1 or NM in case of bcc Fe leads to a change from the mechanically stable FM bcc state with $C' > 0$ to the mechanically unstable NM and AFM1 states with $C' < 0$. In the AFM2 state the cubic symmetry is broken even for $c/a = 1$ and the state is unstable for both bcc and fcc structures. It can be therefore concluded, that the type of magnetic state (ferromagnetic, antiferromagnetic or nonmagnetic) has a decisive influence on the overall energetics of phases including their elasticity and thermodynamic stability.

Stability with respect to Stoner-like excitations in bcc FM Fe. For bcc Fe, the change of the magnetic state from FM to NM, which implies a change from a mechanically stable ($C' > 0$) to a mechanically unstable state ($C' < 0$) region, has similarities to so-called Stoner excitations, which are characterized by a reduction of the local magnetic moment. In the following we analyze the gradual changes of the mechanical stability of bcc FM Fe phase and identify a threshold value of the local magnetic moment which separates stable and unstable regions.

The changes can be analyzed based on the total energy difference dE between the cubic ($c/a = 1$) bcc FM state and a representative distorted state (here $c/a = 1.05$). An advantage provided by this approach is that the total energy difference becomes numerically much more robust as compared to the C' elastic constant, particularly in the vicinity of the threshold region which separates the mechanically stable and unstable states. The calculated dE maps are shown as a function of volume and the local magnetic moment in **Fig. 9**. A positive value of dE corresponds to mechanically stable state, while a negative one indicates mechanically unstable region. The identified threshold value of the local magnetic moment only weakly depends on the volume, and is calculated to be within 1.2 – 1.3 μ_B over the whole range of the considered volumes.

Stability along the trigonal transformation path. Similar to the case of a tetragonal transformation path, the bcc structure can be distorted trigonally (see Fig. 1) beyond the region with a quadratic dependence of the total energy on strain. This type of distortions is used to calculate the C_{44} elastic constant. The so-called trigonal transformation path connects all phases with cubic symmetry: bcc, fcc and simple cubic (see **Fig. 10**). Within the path the bcc structure is considered as trigonal with the ratio of $c/a = 1$, where c is measured along the [111] direction and a along a direction perpendicular to the [111] direction. If $c/a \neq 1$, the structure becomes trigonal except for $c/a = 2$, when we attain the simple cubic (sc) structure, and $c/a = 4$, which corresponds to the fcc structure (see Fig. 10).

In accordance with the trigonal symmetry of the structures, the different magnetic states which comply with this symmetry can be studied (**Fig. 11**).

We have calculated the total energies for four different magnetic states along the trigonal transformation path (**Fig. 12**) assuming that the atomic volume is equal to the experimental volume of α–Fe. The symmetry-dictated extrema exist for all four studied states: for the bcc lattice

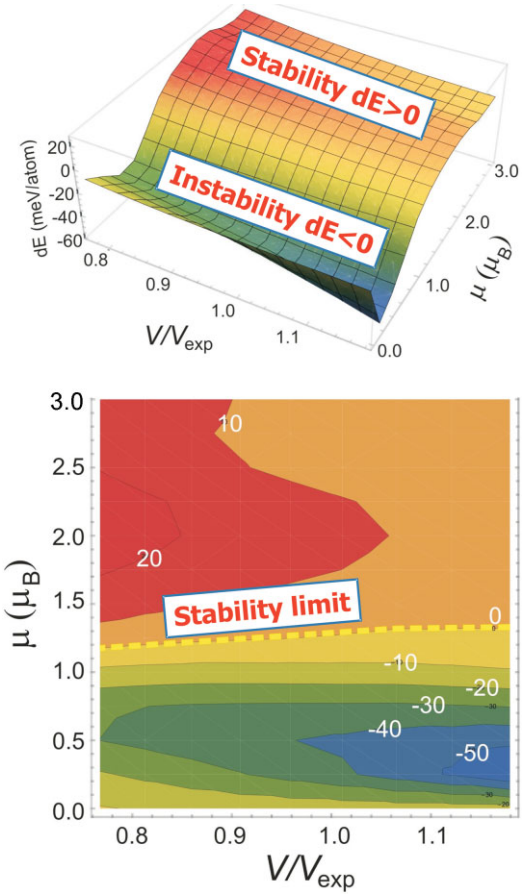

Figure 9. Total energy difference dE between the energy of ferromagnetic bcc Fe and a state with 5% tetragonal distortion as a function of the volume (relative to the experimental equilibrium value) and the local magnetic moment. The energy is shown both as a surface and a contour-plot projection on the basal plane with the contour-plot lines separated by 10 meV/atom. The calculations have been performed using the Vienna Ab-initio Simulation Package (VASP) code [34, 35, 53].

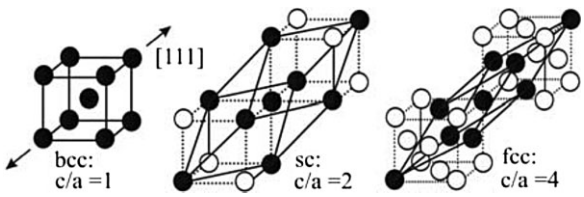

Figure 10. Schematic visualization of the trigonal transformation path transforming the bcc phase into the simple cubic (sc) phase and further into the fcc one. The "c" and "a" lattice parameters were conveniently introduced in an analogy to the Bain's path discussed above (Fig. 5).

(minima), the sc lattice (maxima), as well as minima for the fcc lattice in case of FM and NM states. From the character of these extrema we conclude that the C_{44} elastic constant for all four magnetic states of the bcc lattice are positive, and these states, therefore, are mechanically stable with respect to the trigonal strains. The opposite behaviour is observed for the sc lattice.

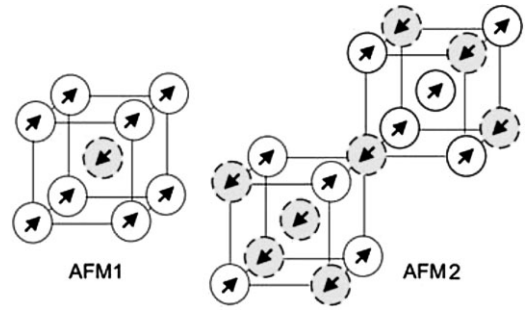

Figure 11. Schematic pictures of two selected antiferromagnetic states (single-layer AFM1 and double-layer AFM2) for the bcc phase studied along the trigonal transformation path. Different orientations of local magnetic moments are indicated by both different shading of spheres representing the atoms and arrows.

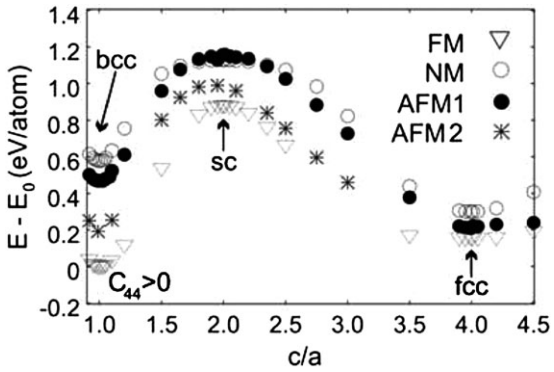

Figure 12. Calculated dependencies of the total energy E (with respect to the energy of the ground state E_0) as a function of the c/a path parameter along the trigonal transformation path.

The results for different volumes can be visualized as a contour-plot of the total energy of the states that have the lowest energy as a function of the *c/a* trigonal-path parameter and volume (**Fig. 13**). The FM state is stable with respect to this distortion in a much broader range of volumes and deformations as compared to the tetragonal deformations (Fig. 8). Studies of other elements or compounds can be found in, e.g., [54–59].

Stability along bcc-hcp transformation path. In conclusion of this section we analyse the bcc-hcp martensitic transformation path (**Fig. 14**). The study was motivated by the fact that bcc iron undergoes a phase transition to a distorted hexagonal-closed-packed (hcp) phase at a pressure of about 13 GPa and this transition has been very intensively studied both experimentally and theoretically [60–77]. Since the hcp–phase is not ferromagnetic and the structural pressure-induced transformation is accompanied by a transition of the magnetic state, four different magnetic states (**Fig. 15**) were simulated in order to clarify the influence of the magnetic degrees of freedom.

A bcc-hcp transformation path can be constructed as a combination of a homogeneous deformation and a shuffling of alternating close-packed atomic planes in opposite

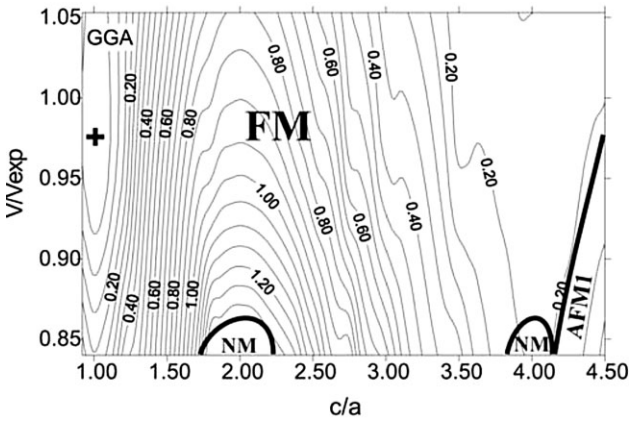

Figure 13. Calculated contour-plot of the total energy E (with respect to the energy of the ground state E_0) as a function of the c/a path parameter and the volume (relative with respect to the experimental volume of α–Fe).The ground state is marked by a cross.

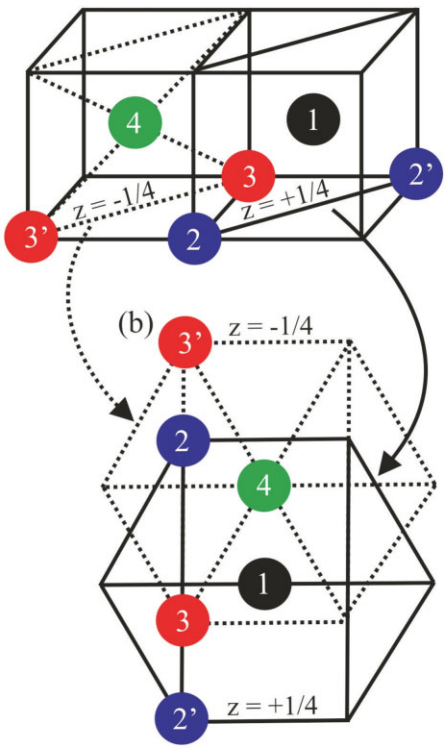

Figure 14. Schematics of the transformation path connecting the bcc and hcp structures. The four-atom basis is distributed over two $(110)_{bcc}$ planes that are continuously deformed and shufed to form two parallel $(0001)_{hcp}$ atomic layers. In (a), two atoms (numbered as 1 and 4) are located at the cube centers, the other two (numbered as 2 and 3) at the cube corners (the atoms 2' and 3' are equivalent to atoms 2 and 3, respectively). The positions of the $(0001)_{hcp}$ planes along the $(0001)_{hcp}$ direction inside the hcp unit cell are indicated by the parameter z equal to either 1/4 or 3/4 (in units of the lattice parameter c).

directions (see, e.g., Ref. [78] or Fig. 14). These two degrees of freedom can be coupled to obtain a single (one) parameter which fully describes this transformation path. The

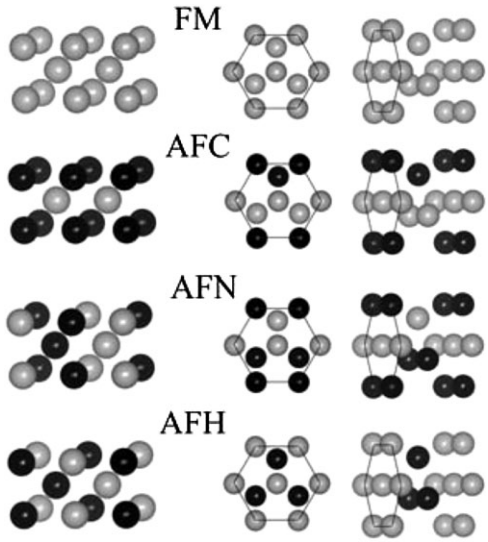

Figure 15. Schematic view of the ferromagnetic and three different anti-ferromagnetic arrangements discussed in the text. The light and dark circles denote atoms with opposite spin orientations (up and down), respectively. Left column shows the bcc-based congurations; the middle column and the right column display the hcp-based arrangements along the $(0001)_{hcp}$ direction and from the side, respectively. Ferromagnetic (FM), antiferromagnetic cubic-symmetry (AFC), antferromagnetic hexagonal (AFH), and antiferromagnetic non-cubic/ non-hexagonal (AFN) indicate different magnetic arrangements considered.

considered path is very similar to the recently proposed path [79–81] that corresponds to linearly increasing strain in two crystallographic directions (while preserving the volume) and shuffling adjacent close-packed planes, with the shuffling being linearly coupled to the magnitude of the strain. Similar paths were proposed also by Craievich *et al.* [82]. All of these one-parameter paths avoid high-energy configurations that are encountered if (i) only a shuffling or (ii) only a lattice deformation is applied, and are close to the minimum energy paths at constant volume.

Along the bcc-hcp transformation path, described below by the parameter p, we consider the bcc and hcp structures, as well as the structures in-between, as orthorhombic with four atoms in the unit cell. The path parameter p is rescaled such that $p = 1$ corresponds to the bcc structure, similarly to the cases of the tetragonal and trigonal paths. $p = \sqrt{2}$ corresponds to the hcp structure, similarly to the fcc structure along the Bain's transformation path.

In **Fig. 16** we present the profiles of the total energy E of the NM, FM, AFC, and AFN arrangements (see Fig. 15) along the bcc-hcp transformation path, calculated with constant atomic volume equal to that of experimental ground state of FM bcc iron. Similarly, as in the case of the bcc–fcc transformation path, the results allow to identify the total energy extrema which are due to the existence of crystal structures with the symmetry higher than orthorhombic. The total energies of the FM and NM phases exhibit extrema for both the bcc and the hcp structures, i.e., at $p = 1$ and $p = \sqrt{2}$,

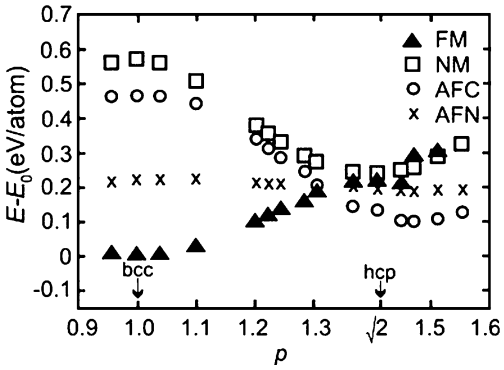

Figure 16. Changes of the total energies along the constant-volume bcc-hcp transformation path calculated with respect to the ground-state energy of ferromagnetic (FM) bcc iron E_0 as a function of the path parameter p (see details in Ref. [78]). The energies of the FM, the non-magnetic (NM), and the two antiferromagnetic states (AFC and AFN) are presented. The results correspond to the experimental atomic volume of bcc FM Fe.

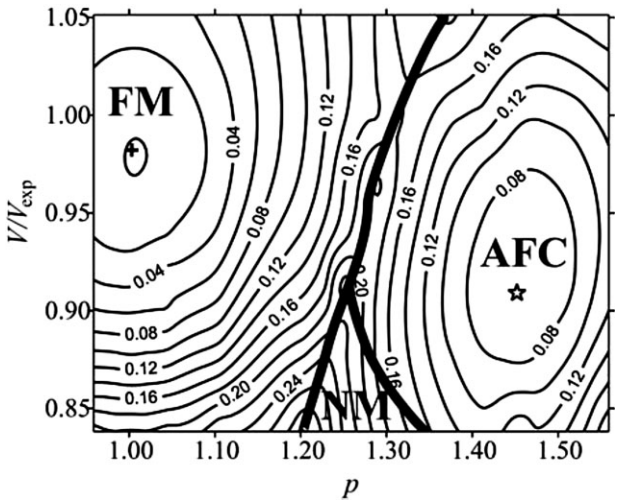

Figure 17. Calculated contour-plot of the total energy E (with respect to the energy of the ground state E_0) as a function of the path parameter p and the volume (relative with respect to the experimental volume of α–Fe). The minima of the ferromagnetic (FM) state and anti-ferromagnetic state with cubic symmetry (AFC) are shown as a full cross and an empty star, respectively.

respectively. The type of these extrema is, however, opposite: a maximum for the FM states corresponds to a minimum for the NM states and vice versa. The total energy of the antiferromagnetic AFC phase exhibits a symmetry-dictated extremum too, i.e., a maximum at $p = 1$. In contrast, the other extremum (minimum at $p = 1.49$) is not dictated by symmetry.

We also show that the transformation path can be divided into regions with different stable magnetic states by minimizing the total energy of the lattice. The FM state has the lowest energy for $p \leq 1.31$, while the AFC state is energetically the most stable for $p > 1.31$. Thus, the resulting minimum total energy profile has a cusp at the point where the FM and AFC curves cross. At $p = \sqrt{2}$, the AFC phase does not exhibit a higher symmetry in comparison to the neighbouring structures along the transformation path and, indeed, no extremum in the total energy of this phase is observed here. The first derivative of the total energy with respect to the path parameter is, therefore, nonzero. Consequently, the hcp phase with this magnetic arrangement is unstable with respect to the transformations along the considered transformation path.

In order to obtain a comprehensive overview of the structural transformation, as well as details of the competition between the different magnetic states, the total energy dependence was calculated along the bcc-hcp transformation path for nine different volumes covering the range from $V/V_{exp} = 0.84$ to $V/V_{exp} = 1.05$. The contour plots of the total energies are shown in **Fig. 17**. Only the states with the lowest total energy are depicted together with the phase boundaries. The calculated ground-state corresponds to bcc FM state at $V/V_{exp} = 0.985$ and $p = 1$.

The total energy minimum of the AFC state is located at the point $V/V_{exp} = 0.909$ (71.9 a.u.^{3}/atom), $p = 1.46$, and is not symmetry dictated. The corresponding total energy is higher than that of the equilibrium FM bcc phase by 0.064 eV/atom. Again, phase boundaries separating stable ferromagnetic (FM) states from regions with either the nonmagnetic (NM) or the antiferromagnetic AFC-type allow to identify the region of stability of the FM phase. For recent studies of bcc-hcp transformation in Fe see e.g., [83, 84].

Tensile Test Simulations Up to the Tensile Strength and Beyond

After examining the elasticity of iron and its behaviour along volume conserving tetragonal, trigonal and bcc-hcp transformation paths, we focus now on deformation processes that do not conserve volume. This is e.g. the case for tensile tests. Specifically, (i) the uniaxial tensile tests along the [001] and [111] directions will be simulated including Poisson's contractions in directions perpendicular to the loading direction, as well as (ii) triaxial loading conditions. Due to the fact that the applicability of quantum-mechanical approaches is not limited to states close to the ground state, extreme loading conditions may be simulated up to the materials strength limits and even beyond it. In this way, the theoretical tensile strength, corresponding to the fracture of an ideal, defect free crystal, can be determined. The theoretical tensile strength is experimentally very difficult to attain and the only materials in which it was approached in the past are whiskers of very pure metals and silicon [85–87], which are practically dislocation free. However, recent developments in materials engineering, such as the production of defect-free thin films and the advancement of various nanostructured materials, have stimulated interest in studies of the ideal strength which in these materials may control both the onset of fracture and the dislocation nucleation, as demonstrated by nanoindentation experiments (see, e. g., Refs. [88–95]).

Theoretically, the ideal strength can again be investigated using density functional theory. Importantly, each loading mode has its own theoretical strength and as the values of theoretical tensile strength for different loading types represent the limits of materials stability, the lowest one is the most relevant for the onset of dislocations motion. The corresponding loading mode is the weakest link when analyzing a complex distorted environment of dislocation cores, grain boundaries, and other extended defect with decisive impact on materials plasticity and strength. A few selected examples of different loading conditions are summarized below.

Uniaxial tensile test simulation. The first paper dealing with ideal tensile strength calculated with the first principles approach was that of Esposito *et al.* [96], who used unrelaxed structures for Cu. Later, Paxton *et al.* [97] and Xu and Moriarty [98] calculated shear strength for unrelaxed shear deformation. Probably the first *ab initio* simulation of a tensile test, including the relaxation in perpendicular direction to the loading axis, was performed by Price *et al.* [99] for uniaxial loading of TiC along the [001] axis. Later, systematic *ab initio* studies of theoretical strength and stability in metals and intermetallic compounds under extreme conditions were initiated in the group of M. Šob, starting with the theoretical tensile strength for [001] and [111] loading axes in tungsten (see Ref. [100]). Since then, tensile tests were simulated for numerous crystalline materials (see, e.g., [101–104]) and their theoretical tensile strengths were determined (for a review before the year 2005 see e.g. [105, 106]).

To simulate a uniaxial tensile test, we start by determining the structure and total energy of the material in the ground state. In the second step, we elongate the structure along the loading axis by a fixed amount ε_3, what is equivalent to applying a certain tensile stress σ_3. For each value of ε_3 we minimize the total energy by relaxing the stresses σ_1 and σ_2 in the directions perpendicular to the loading axis. The stress σ_3 is given by

$$\sigma_3 = \frac{c}{V}\frac{\partial E}{\partial c} = \frac{1}{Ac_0}\frac{\partial E}{\partial \varepsilon_3}, \qquad (5)$$

where E is the total energy per computed unitcell or supercell, V is the volume of the cell, c is the dimension of the cell in the direction of loading, A (equal to V/c ratio) is the area of the basis of the cell in the plane perpendicular to the loading axis, and c_0 is the value of c in the undeformed state.

The inflexion point in the dependence of the total energy on the elongation yields the maximum of the tensile stress during loading. If any other instability (violation of some stability condition, soft phonon modes, magnetic spin arrangement *etc.* [95, 107–116]) does not occur prior to reaching this inflexion point, the maximum of the tensile stress corresponds to the theoretical tensile strength, σ_{th}. In principle, analysis of the phonon spectrum of a strained crystal at each point of the deformation path is necessary and sufficient to ascertain the stability of the investigated material. Such an analysis based on *ab initio* calculations is, however, extremely demanding, and was performed only for tensile tests in Al [117]. A detailed description of *ab initio* calculations of theoretical tensile strength and a review of recent results may be found in Refs. [118, 119]. *Ab initio* calculations of theoretical tensile and shear strength are also reviewed in e.g. Ref. [118].

In accordance with the methodology described above, we performed the simulation of a tensile test in iron for uniaxial loading along the [001] and [111] directions, respectively. The corresponding total energies as functions of relative elongation ε are displayed in **Fig. 18(a)**. It is seen from Fig. 18(a) that the total energy profiles have a parabolic, convex character in the neighborhood of the ferromagnetic, symmetry-dictated, minimum which corresponds to the bcc structure (ground state). With increasing value of ε the curves reach (due to non-linear effects) their inflexion points (marked by vertical lines in Fig. 18(a)), which correspond to the maximum stress in the material and become concave. The actual values are summarized in **Tab. 2**.

The tensile stresses calculated according to the Eq. (5) are shown in Fig. 18(c). The inflexion points on the total energy profiles (Fig. 18(a)) correspond to maximum stresses (Fig. 18(c)) which the material can accommodate if its structure type does not change during the deformation. For uniaxial tensile test along the [001] and [111] directions they are equal to $\sigma^{max}_{[001]} = 12.7$ GPa (this value was reported in our previous work (Refs. [120, 121])) and is similar to the values of 14.2 and 12.6 GPa found in Refs. [111, 122], respectively, and $\sigma^{max}_{[111]} = 27.3$ GPa (Refs. [110, 121]). These values represent the theoretical tensile strengths provided other instabilities do not come forth before the inflexion point has been reached.

The maxima on the total energy versus ε dependence are dictated by symmetry (Fig. 18(a)). They correspond to fcc and simple cubic structures when simulating tensile tests with loading along the [001] and [111] directions, respectively. These maxima are denoted by arrows in Fig. 18(a). Their presence indicates that the corresponding dependence of the energy on elongation must level off, which imposes certain limitations on the maximum stress. In cases when there is no symmetry-dictated maximum (e.g., in the uniaxial tensile test along the [001] direction of NiAl with the B2 structure in the ground state [123]), the maximum stress is usually higher.

Since the structural energy difference $E_{sc} - E_{bcc}$ is about five times higher than the difference $E_{fcc} - E_{bcc}$ (755 meV/atom compared to 155 meV/atom), the E versus ε curve for the [111] loading must rise much higher, albeit for larger strains, than that for the [001] loading (see Fig. 18(a)). Consequently, for the tensile test in the [111] direction the inflexion point occurs at a higher strain and for a higher stress than in the test with loading in the [001] direction. Thus, similarly as for W [98], a marked anisotropy of ideal tensile strengths for the [001] and [111] loading directions may be understood in terms of the structural energy differences of nearby higher-symmetry structures found along the deformation path.

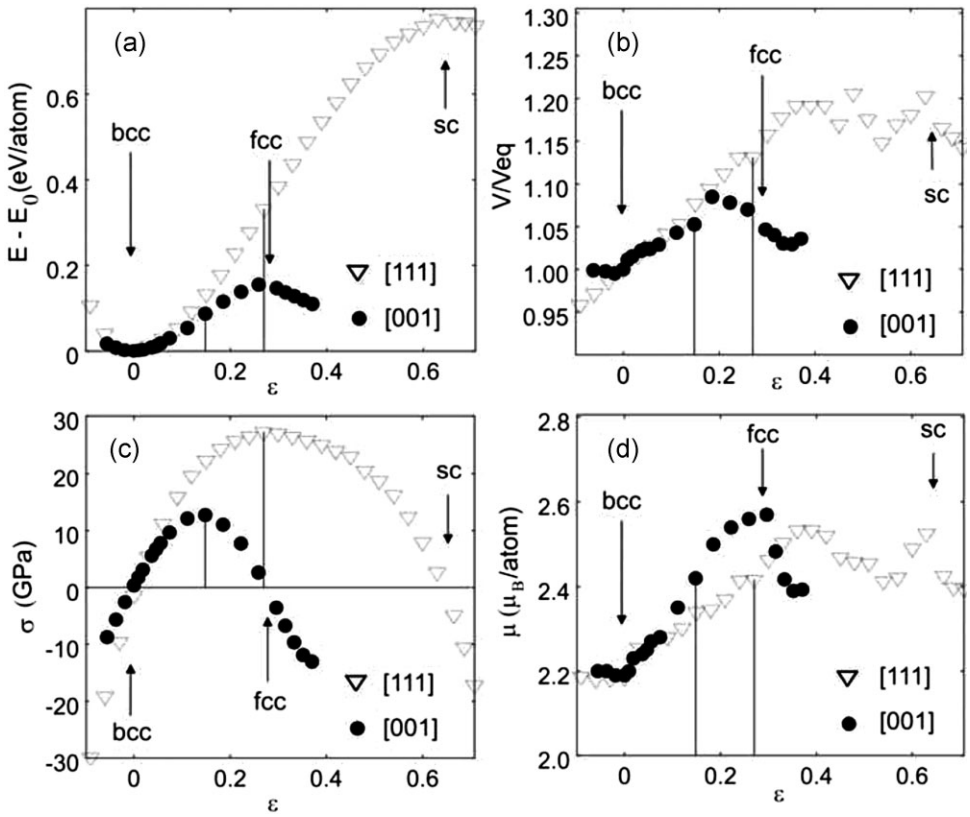

Figure 18. (a) Total energy per atom relative to the energy of the equilibrium state, (b) relative atomic volume ratio with respect to the equilibrium volume V_{eq}, (c) calculated tensile stress in the material, and (d) magnetic moment per atom of ferromagnetic iron loaded uniaxially along the [001] and [111] directions versus elongation ε. The relative elongation ε reflects the increase or decrease of the crystal dimension in the direction of loading. The vertical thin lines show the states exhibiting maximum stress (i.e,. the theoretical tensile strength).

Relative changes of atomic volume and the dependences of the magnetic moment of FM iron are shown as functions of elongation in Fig. 18(b) and (d), respectively. In the vicinity of the ground state structure the atomic volume increases with increasing elongation, but it exhibits a more complex behavior at larger deformations.

Triaxial (isotropic) loading simulation. We complete the section with the triaxial loading simulations [124] in which the strain ε corresponds to a relative extension of the bcc lattice parameter a. The volume of the unit cell is isotropically expanded in all directions corresponding to the application of negative hydrostatic pressure. The triaxial stress is calculated as

$$\sigma = \frac{\partial E}{\partial V}. \qquad (6)$$

Table 2. Theoretical tensile strengths of α-Fe for loading along the [001] and [111] directions together with the value obtained from triaxial loading conditions.

	[001]	[111]	triaxial
Theoretical tensile strength σ^{th} (GPa)	12.7	27.3	27.9

The corresponding total energies as functions of relative elongation ε are displayed in **Fig. 19(a)**. The total energy profiles have a parabolic, convex character in the vicinity of the ground state volume. With increasing value of ε the total-energy curve reaches its inflexion point (marked by vertical lines in Fig. 19(a)) and becomes concave. The inflexion point for the isotropic triaxial loading occurs (most likely incidentally) for nearly the same elongation of $\varepsilon = 0.15$ as in the case of the [001] tensile test. This elongation corresponds to the bcc structure with the lattice constant of 6.20 a.u.

The triaxial tensile stresses calculated according to Eq. (6) are shown in Fig. 19(c). The inflexion point on the total energy proles (Fig. 19(a)) corresponds to maximum stress of $\sigma^{max} = 27.9$ GPa [101, 121] (see Fig. 19(c)). It should be noted that the theoretical strength for hydrostatic loading is nearly the same as that obtained for the loading in the [111] direction, 27.3 GPa. At present, we do not have any plausible explanation of this fact. In agreement with Herper *et al.* [49], the magnetic moment shows monotonous increase with increasing volume (Fig. 19(b)). (This is in contrast to the behavior during the uniaxial tensile tests, where local extrema at points corresponding to higher-symmetry structures (maxima for fcc and simple cubic), as well as at some other points along the transformation paths, exist.

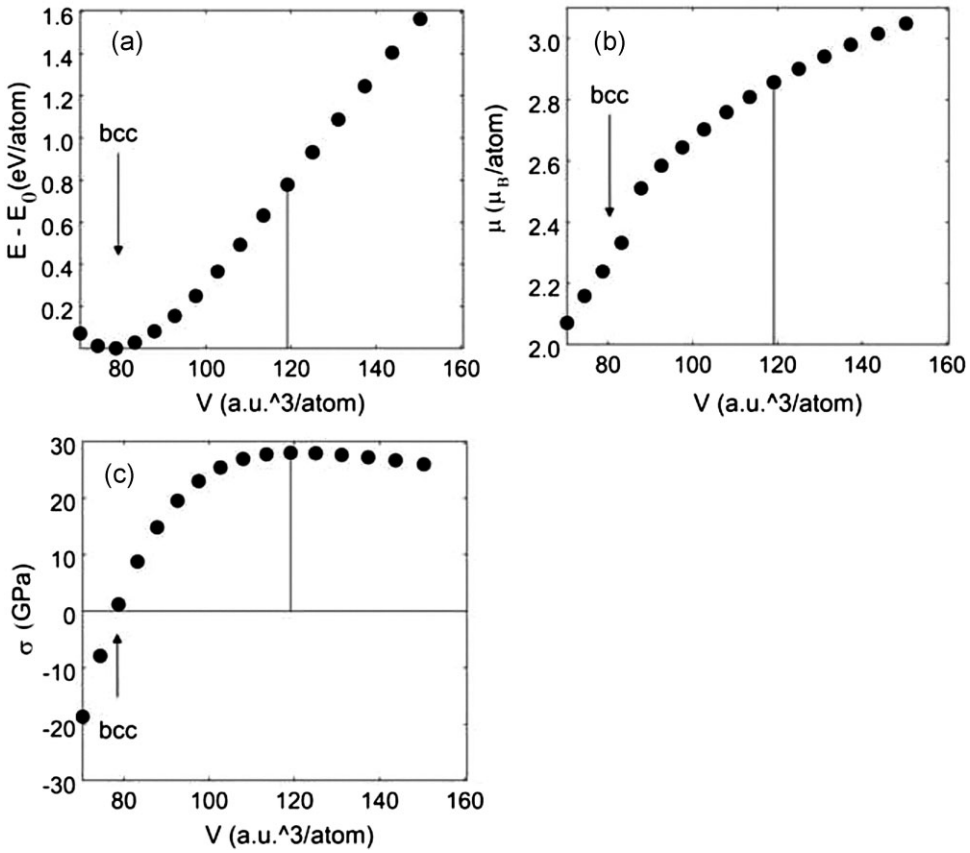

Figure 19. (a) Total energy per atom relative to the energy of the equilibrium state, (b) magnetic moment per atom of ferromagnetic iron, (c) calculated triaxial tensile stress in the bcc ferromagnetic Fe.

Analyzing all three different loading conditions and corresponding theoretical tensile strengths we conclude, that, unless another process with a yet lower strength is active, the theoretical tensile strength for uniaxial loading along the [001] direction is the upper limit of attainable stresses in ferromagnetic bcc Fe. This value can be compared with those determined for a variety of other materials for which similar analysis was recently performed for pure elements [125–138], intermetallics [139–146], or, e.g., graphene layers [147], under uniaxial loading conditions, biaxial loads [148, 149], hydrostatic pressures [150, 151], or grain boundaries [152].

Summary and Outlook

In this paper, quantum-mechanical calculations were applied to elemental ferromagnetic bcc Fe, specifically for the determination of its ground-state elastic constants and polycrystalline moduli. A detailed study of its magnetism including Stoner-like excitations and influence of different magnetic states on tetragonal, trigonal and bcc-hcp transformation paths that resulted in the identification of the stability limits of the FM state with respect to different phase transformations was presented. The study has been complemented with simulations of iron's response to extreme loading conditions such as uniaxial and triaxial tensile tests in order to identify theoretical tensile strengths of α-Fe. We note that these calculations are not limited to pure elements or existing materials and may thus also provide data on the atomic scale that are inaccessible experimentally. This is related to the fact that not only the ground-state properties, but also materials response to extreme loading conditions can reliably be determined.

More generally, *ab initio* approaches to the elasticity of materials can be used within a theory-guided materials design of alloys and composites with properties dictated by a specific (industrial) need. The theory-guided materials design allows prediction of selected materials properties (such as elastic constants or moduli) of new materials without actually synthesizing them. According to this philosophy, the most promising phase(s) and composition(s) are selected and the samples are synthesized and tested only for these theoretically pre-selected materials. Such a combined, theoretical and experimental, approach leads to an optimized materials design within significantly shorter time and at reduced costs when compared to the conventional, solely experimental, materials development.

We complete the paper with an example of such a materials design aiming at specific elastic properties of alloys. In contrast to many top-down approaches that start from the macroscopic scale and continue downscale, a quantum-mechanics-based bottom-up approach is chosen

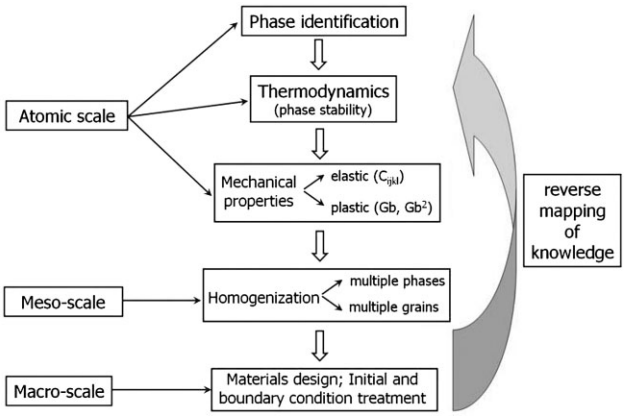

Figure 20. Schematic overview of our multi-scale and multi-disciplinary strategy combining (i) thermodynamic phase-stability and (ii) single-crystalline elasticity data obtained at atomic level by first-principles calculations with self-consistent homogenization techniques in order to bridge scale differences.

here to identify more rapidly both suited compositions with regard to the thermodynamic stabilization of the desired phase as well as to scrutinize some of the basic structural and mechanical features of possible alloy candidates (see **Fig. 20**).

First, the thermodynamic stability for a variety of phases is determined in order to identify the stable one(s) as well as their volumetric ratio in a multi-phase alloy if necessary. Together with the thermodynamic stability of phases, the mechanical stability is tested by computing single-crystalline elastic constants. Second, polycrystalline elastic moduli and other engineering parameters measurable at macroscale were predicted employing linear-elasticity homogenization techniques that allow scale-bridging between atomistic and macroscopic levels.

Starting from an initial composition and based on the residuum/deviation of the properties on the macroscale a new atomic composition is suggested and studied. This cycle is repeated until the desired properties are obtained. Following this strategy, an alloy composition with desired properties is obtained. Of course, if the properties are not accessible by any chemical composition, new phases/compositions or properties have to be identified.

Such a theory-guided materials design has successfully been applied to a wide range of materials (see for example Refs. [71–78]). When aiming at materials with specific elastic properties, a few recent cases can be mentioned, (i) the development of new Ti-based biocompatible Ti-Nb and Ti-Mo alloys intended for medical application (implant materials), (ii) ultra light-weight Mg-Li alloys, and (iii) elasticity tuning of the so-called MAX phases (ternary nanolaminated transition metal carbides or nitrides) [153–155]. In the case of Ti alloys, an alloy composition providing significantly reduced Young's modulus (matching that of human bone) was searched for. The study was carried out to prevent negative stress-shielding effect that is observed in implants that are too stiff as compared with the bone [156].

In the case of Mg-Li alloys, an optimum alloy was sought for that represents a compromise between two conflicting criteria (i) specific Young's modulus as a measure of strength, and (ii) the bulk over shear modulus ratio as an approximate indicator [157] of either brittle or ductile behavior (see e.g. [16–25]). Importantly, the on-going developments in both quantum-mechanical methods and atomistic and/or continuum approaches to modeling of materials properties show many promising trends towards further extension of the above mentioned multi-scale and multi-disciplinary schemes beyond the elasticity of materials into the field of their complex plasticity behavior (see, e.g., [158–160]) and/or finite temperatures via taking into account e.g. vibronic degrees of freedom (see for example[161–165]) or magnetic excitations (see e.g. [166–178]).

Acknowledgements

We would like to acknowledge financial support of the collaborative research center SFB 761 "Stahl*ab initio*" of the Deutsche Forschungsgemeinschaft and funding by the Interdisciplinary Centre for Materials Simulation (ICAMS), which is supported by ThyssenKrupp AG, Bayer MaterialScience AG, Salzgitter Mannesmann Forschung GmbH, Robert Bosch GmbH, Benteler Stahl/Rohr GmbH, Bayer Technology Services GmbH and the state of North-Rhine Westphalia as well as the European Commission in the framework of the European Regional Development Fund (ERDF). M. Š. would like to acknowledge financial support by the Research Projects Nos. AV0Z20410507 and IAA100100920 of the Academy of Sciences of the Czech Republic, Project No. MSM0021622410 of the Ministry of Education of the Czech Republic and Project No. 202/09/1786 of the Grant Agency of the Czech Republic. The access to the METACentrum computing facilities provided under the Research Project MSM6383917201 is greatly appreciated. We would also like to thank David Holec from the Department of Physical Metallurgy and Materials Testing, Montanuniversität Leoben, Austria, for many fruitful discussions related to the design of special quasi-random structures.

References

[1] P. Hohenberg, W. Kohn: Phys. Rev. 13 (1964) B864.
[2] W. Kohn, L. J. Sham: Phys. Rev. 140 (1965) A1133.
[3] D. Ma, M. Friák, D. Raabe, J. Neugebauer, F. Roters: Phys. Stat. Sol. b 245 (2008) 2642.
[4] F. Roters, P. Eisenlohr, L. Hantcherli, D. D. Tjahjanto, T. R. Bieler, D. Raabe: Acta Mater. 58 (2010) 1152.
[5] D. Music, F. H.-U. Basse, R. Haßdorf, J. M. Schneider: J. Appl. Phys. 108 (2010) 013707.
[6] A. E. Mattsson, P. A. Schultz, M. P. Desjarlais, T. R. Mattsson, K. Leung: Modeling Simul. Mater. Sci. Eng. 13 (2005) R1.
[7] J. A. Moriarty, L. X. Benedict, J. N. Glosli, R. Q. Hood, D. A. Orlikowski, M. V. Patel, P. Söderlind, F. H. Streitz, M. Tang, L. H. Yang: J. Mater. Res. 21 (2006) 563.
[8] Handbook of Materials Modeling, ed. S. Yip, (Ed.) (Dordrecht, Berlin, Heidelberg, New York, Springer, 2005.
[9] Proceedings of the Third Int. Conf. on Multiscale Materials Modeling, ed. P. Gumbsch, Stuttgart: Fraunhofer IRB, 2006.

[10] K. Chen, L. R. Zhao, J. S. Tse: J Appl Phys. 93 (2003) 2414.
[11] P. Söderlind, O. Eriksson, J. M. Wills, A. M. Boring: Phys. Rev. B 48 (1993) 5844.
[12] F. D. Murnaghan: Proc. Natl. Acad. Sci. USA 30 (1944) 244.
[13] W. Voigt, Lehrbuch der Kristallphysik, Leipzig Germany, (Teubner, Stuttgart, 1928).
[14] A. Z. Reuss: Angew. Math. Mech. 9 (1929) 49.
[15] A. V. Hershey: J. Appl Mech 21 (1954) 236.
[16] G. Ghosh, S. Delsante, G. Borzone, M. Asta, R. Ferro: Acta Mater. (2006) 54 4977.
[17] M. Friák, W. A. Counts, D. Raabe, J. Neugebauer: Phys. Stat. Sol. b 245 (2008) 2636.
[18] W. A. Counts, M. Friák, D. Raabe, J. Neugebauer: Acta Mater. 57 (2009) 69.
[19] W. A. Counts, M. Friák, D. Raabe, J. Neugebauer: in: Magnesium, 8th International Conference on Magnesium Alloys and their Applications (Edited by K. U. Kainer,) WILEY-VCH, Weinheim, 2009, 133.
[20] W. A. Counts, M. Friák, D. Raabe, J. Neugebauer: Adv. Eng. Mat. 12 (2010) 572.
[21] W. A. Counts, M. Friák, D. Raabe, J. Neugebauer: Adv. Eng. Mat. (2010), in press
[22] M. Friák, J. Deges, R. Krein, G. Frommeyer, J. Neugebauer: Intermetallics. 18 (2010) 1310.
[23] M. Friák, J. Deges, F. Stein, M. Palm, G. Frommeyer, J. Neugebauer, in Advanced Intermetallic-Based Alloys for Extreme Environment and Energy Applications, edited by M. Palm, B.P. Bewlay, M. Takeyama, J.M.K. Wiezorek, Y-H. He, (Mater. Res. Soc. Symp. Proc. Volume 1128, Warrendale, PA, 2009), p. 59.
[24] W. A. Counts, M. Friák, C. C. Battaile, D. Raabe, J. Neugebauer: Phys. Stat. Sol. b 245 (2008) 2630.
[25] J. Z. Liu, A. van de Walle, G. Ghosh, M. Asta: Phys. Rev. B 72 (2005) 144109.
[26] J. M. Sanchez, F. Ducastelle, D. Gratias: Physica A 128 (1984) 334.
[27] P. Soven: Phys. Rev. 156 (1967) 809.
[28] D. B. Laks, L. G. Ferreira, S. Froyen, A. Zunger: Phys. Rev. B 46 (1992) 12587.
[29] J. von Pezold, A. Dick, M. Friák, J. Neugebauer: Phys. Rev. B 81 (2010) 094203.
[30] W. C. Hubbell, F. R. Brotzen: J. Appl. Phys. 43 (1972) 330.
[31] L. Vitos: Phys. Rev. B 64 (2001) 014107.
[32] A. van de Walle, M. Asta: Modelling Simul. Mater. Sci. Eng. 10 (2002) 521.
[33] A. van de Walle, M. Asta, G. Ceder: CALPHAD 26 (2002) 539.
[34] G. Kresse, J. Furthmüller: Phys. Rev. B 54 (1996) 11169.
[35] G. Kresse, J. Hafner: Phys. Rev. B 47 (1993) 558.
[36] D. Music, T. Takahashi, L. Vitos, C. Asker, I. A. Abrikosov, J. M. Schneider: Appl. Phys. Lett. 91 (2007) 191904.
[37] D. Music, S. Konstantinidis, J. M. Schneider: J. Phys. : Condens. Matter 21 (2009) 175403.
[38] I. A. Abrikosov, S. I. Simak, B. Johansson, A. V. Ruban, H. L. Skriver: Phys. Rev. B 56 (1997) 9319.
[39] P. Alippi, P. M. Marcus, M. Scheffler: Phys. Rev. Lett. 78 (1997) 3892.
[40] M. Šob, L. G. Wang, V. Vitek: Comput. Mater. Sci. 8 (1997) 100.
[41] V. Paidar, L. G. Wang, M. Šob, V. Vitek: Modell. Simul. Mater. Sci. Eng. 7 (1996) 369.
[42] J. P. Perdew, S. Burke, M. Ernzerhof: Phys. Rev. Lett. 77 (1996) 3865.
[43] P. Blaha, K. Schwarz, J. Luitz: WIEN97, Technical University of Vienna, 1997 (improved and updated Unix version of the original copyrighted WIEN code, which was published by P. Blaha, K. Schwarz, P. Sorantin, and S. B. Trickey, in Comput. Phys. Commun. 59, 399 (1990)).
[44] M. M. Shukla: J. Phys. D, Appl. Phys. 15 (1982) L177.
[45] M. Friák, M. Šob, V. Vitek: Phys. Rev. B 63 (2001) 052405.
[46] L. Stixrude, R. E. Cohen, D. J. Singh: Phys. Rev. B 50 (1994) 6442.
[47] E. G. Moroni, G. Kresse: J. Hafner: Phys. Rev. B 56 (1997) 15629.
[48] C. Elsässer, J. Zhu, S. G. Louie, M. Fähnle, C. T. Chan: J. Phys. : Condens. Matter 10 (1998) 5081; 10 (1998) 5113.
[49] H. C. Herper, E. Hoffmann, P. Entel: Phys. Rev. B 60 (1999) 3839.
[50] S. L. Qiu, P. M. Marcus, H. Ma: J. Appl. Phys. 87 (2000) 5932.
[51] D. Spišák, J. Hafner: Phys. Rev. B 61 (2000) 16129.
[52] P. J. Craievich, M. Weinert, J. M. Sanchez, R. E. Watson: Phys. Rev. Lett. 72 (1994) 3076.
[53] P. E. Blöchl: Phys. Rev. B 50 (1994) 17953.
[54] M. Šob, D. Legut, M. Friák, J. Fiala: J. Magn. Magn. Mat. 272-276 (2004) e205.
[55] M. Šob, M. Friák, D. Legut, and V. Vitek: In Complex Inorganic Solids - Structural, Stability, and Magnetic Properties of Alloys, eds. P. E. A, Turchi, A, Gonis, K, Rajan, and A. Meike, Springer-Verlag, Berlin-Heidelberg-New York, 2005, pp. 307–326.
[56] M. Friák, A. Schindlmayr, M. Scheffler: New J. Phys. 9 (2007) 5.
[57] D. Legut, M. Friák, M. Šob: Phys. Rev. Lett. 99 (2007) 016402.
[58] D. Legut, M. Friák, M. Šob: Phys. Rev. B 81 (2010) 214118.
[59] M. Zelený, M. Šob: Phys. Rev. B 77 (2008) 155435.
[60] D. Bancroft, E. Peterson, S. Minshall: J. Appl. Phys. 27 (1956) 291.
[61] F. M. Wang, R. Ingalls: Phys. Rev. B 57 (1998) 5647.
[62] Y. Chen, K. M. Ho, B. N. Harmon: Phys. Rev. B 37 (1988) 283.
[63] I. A. Abrikosov, P. James, O. Eriksson, P. Söderlind, A. V. Ruban, H. L. Skriver, B. Johansson: Phys. Rev. B 54 (1996) 3380.
[64] M. Ekman, B. Sadigh, K. Einarsdotter, P. Blaha: Phys. Rev. B 58 (1998) 5296.
[65] D. F. Johnson, E. A. Carter: J. Chem. Phys. 128 (2008) 104703.
[66] J. B. Liu, D. D. Johnson: Phys. Rev. B 79 (2009) 134113.
[67] G. L. Krasko, B. Rice, S. Yip: J. Comput. -Aided Mater. Des. 6 (1999) 129.
[68] G. Steinle-Neumann, L. Stixrude, R. E. Cohen: Phys. Rev. B 60 (1999) 791.
[69] M. Šob, M. Friák, L. Wang, and V. Vitek, Multiscale Modelling of Materials, edited by In: V. Bulatov, T.D. de Rubia, R. Phillips, E. Kaxiras, N. Ghoniem, MRS Symposia Proceedings No. 538 (Materials Research Society, Pittsburgh, 1999), pp. 523–527.
[70] M. Šob, M. Friák, L. Wang, V. Vitek, in Proceedings of the International Conference on Solid-Solid Phase Transformations '99 (JIMIC-3), edited by M. Koiwa, T. Otsuka, T. Miyazaki, (The Japan Institute of Metals, Sendai, 1999), pp. 855–858.
[71] M. Šob, M. Friák: Kovové Mater. (Metallic Materials) 38 (2000) 225.
[72] D. Spišák, R. Lorenz, J. Hafner: Phys. Rev. B 63 (2001) 094424.
[73] K. J. Caspersen, A. Lew, M. Ortiz, E. A. Carter: Phys. Rev. Lett. 93 (2004) 115501.
[74] G. Steinle-Neumann, R. E. Cohen, L. Stixrude: J. Phys. : Condens. Matter 16 (2004) S1109.
[75] G. Steinle-Neumann, L. Stixrude, R. E. Cohen: Proc. Natl. Acad. Sci. USA. 101 (2004) 33.
[76] F. Baudelet, S. Pascarelli, O. Mathon, J. P. Itié, A. Polian, M. d'Astuto, J. C. Chervin: J. Phys. : Condens. Matter 17 (2005) S957.
[77] A. Lew, K. Caspersen, E. A. Carter, M. Ortiz: J. Mech. Phys. Solids 54 (2006) 1276.
[78] M. Friák, M. Šob: Phys. Rev. B 77 (2008) 174117.
[79] V. Paidar, L. Wang, M. Šob, V. Vitek: Modell. Simul. Mater. Sci. Eng. 7 (1999) 369.
[80] M. Mrověc, D. Nguyen-Manh, D. G. Pettifor, V. Vitek: Phys. Rev. B 69 (2004) 094115.
[81] M. Černý, M. Boyer, M. Šob, S. Yip: J. Comput. -Aided Mater. Des. 12 (2005) 161.
[82] P. J. Craievich, J. M. Sanchez, R. E. Watson, M. Weinert: Phys. Rev. B 55 (1997) 787.
[83] J. L. Shao, A. M. He, S. Q. Duan, P. Wang, C. S. Qin: Acta Physica Sinica. 59 (2010) 4888.
[84] Z. P. Lu, W. J. Zhu, T. C. Lu, S. J. Liu, X. L. Cui, X. R. Chen: Acta Physica Sinica. 59 (2010) 4303.
[85] S. S. Brenner: J. Appl. Phys. 27 (1956) 1484.
[86] S. S. Brenner: J. Appl. Phys. 28 (1957) 1023.
[87] R. V. Coleman, B. Price, N. Cabrera: J. Appl. Phys. 28 (1957) 1360.
[88] G. L. Pearson, W. T. Read, Jr., W. L. Feldmann: Acta Metall. 5 (1957) 181.
[89] E. M. Nadgornyi: Usp. Fiz. Nauk 77 (1962) 201 [Sov. Phys. Usp. 5 (1962) 462].
[90] R. P. Vinci, J. J. Vlassak: Annu. Rev. Mater. Sci. 26 (1996) 431.
[91] D. F. Bahr, D. E. Kramer, W. W. Gerberich: Acta Mater. 46 (1998) 3605.
[92] A. Gouldstone, H. J. Koh, K. Y. Zeng, A. E. Giannakopoulos, S. Suresh: Acta Mater. 48 (2000) 2277.
[93] C. L. Woodcock, D. F. Bahr: Scr. Mater. 43 (2000) 783.
[94] O. R. de la Fuente, J. A. Zimmerman, M. A. Gonzalez, J. de la Figuera, J. C. Hamilton, W. W. Pai, J. M. Rojo: Phys. Rev. Lett. 88 (2002) 036101.

[95] K. J. van Vliet, J. Li, T. Zhu, S. Yip, S. Suresh: Phys. Rev. B 67 (2003) 104105.
[96] E. Esposito, A. E. Carlsson, D. D. Ling, H. Ehrenreich, C. D. Gelatt: Jr.: Phil. Mag. 41 (1980) 251.
[97] A. T. Paxton, P. Gumbsch, M. Methfessel: Phil. Mag. Lett. 63 (1991) 267.
[98] W. Xu, J. A. Moriarty: Phys. Rev. B 54 (1996) 6941.
[99] D. L. Price, B. R. Cooper, J. M. Wills: Phys. Rev. B 46 (1992) 11368.
[100] M. Šob, L. G. Wang, V. Vitek: Mat. Sci. Eng. A 234–236. (1997) 1075.
[101] M. Šob, M. Friák, D. Legut, J. Fiala, V. Vitek: Mat. Sci. Eng. A 387–389 (2004) 148.
[102] M. Šob, M. Friák, D. Legut, and V. Vitek, In Complex Inorganic Solids - Structural, Stability, and Magnetic Properties of Alloys, eds. P. E. A. Turchi, A. Gonis, K. Rajan, and A. Meike, Springer-Verlag, Berlin-Heidelberg-New York 2005, pp. 307–326.
[103] M. Friák, M. Šob, V. Vitek: Phys. Rev. B 68 (2003) 184101.
[104] M. Šob, M. Friák: Intermetallics 17 (2009) 523.
[105] F. Milstein, S. Chantasiriwan: Phys. Rev. B 58 (1998) 6006.
[106] P. Šandera, J. Pokluda: Scripta Metall. Mater. 29 (1993) 1445.
[107] W. Li, T. Wang: J. Phys.: Condens. Matter 10 (1998) 9889.
[108] J. W. Morris, Jr., C. R. Krenn: Phil. Mag. A 80 (2000) 2827.
[109] W. Luo, D. Roundy, M. L. Cohen, J. W. Morris Jr.: Phys. Rev. B 66 (2002) 094110.
[110] M. Šob, M. Friák, D. Legut, V. Vitek, in: P. E. A. Turchi, A. Gonis (Eds.), Proceedings of the Third International Alloy Conference: An Interdisciplinary Approach to the Science of Alloys in Metals, Minerals and Other Materials Systems, Estoril/Cascais, Portugal, June 30–July 5, 2002.
[111] D. M. Clatterbuck, D. C. Chrzan, J. W. Morris Jr.: Acta Mater. 51 (2003) 2271.
[112] R. Hill, F. Milstein: Phys. Rev. B 15 (1977) 3087.
[113] J. Wang, J. Li, S. Yip, S. Phillpot, D. Wolf: Phys. Rev. B 52 (1995) 12627.
[114] Z. Zhou, B. Joós: Phys. Rev. B 54 (1996) 3841.
[115] K. Y. Kim: Phys. Rev. B 54 (1996) 6245.
[116] M. Černý, M. Šob, J. Pokluda, P. Šandera: J. Phys.: Condens. Matter 16 (2004) 1045.
[117] D. M. Clatterbuck, C. R. Krenn, M. L. Cohen, J. W. Morris Jr.: Phys. Rev. Lett. 91 (2003) 135501.
[118] J. Pokluda, M. Černý, P. Šandera, M. Šob:, J. of Comp.-Aided Mat. Design 11 (2004) 1.
[119] J.W. Morris, Jr, in Handbook of Materials Modelling, ed. S. Yip, Dordrecht, Berlin, Heidelberg, New York: Springer Verlag, 2005, p. 2777.
[120] M. Friák, M. Šob, V. Vitek: in Proceedings of the International Conference Juniormat'01, Institute of Materials Engineering, Brno University of Technology, Brno, 2001, pp. 117–120.
[121] M. Friák, M. Šob, V. Vitek: Phil. Mag. 83 (2003) 3529.
[122] D. M. Clatterbuck, D. C. Chrzan, J. W. Morris Jr.: Phil. Mag. Lett. 82 (2002) 141.
[123] M. Šob, L. G. Wang, V. Vitek: Phil. Mag. B 78 (1998) 653.
[124] M. Černý, J. Pokluda, M. Šob, M. Friák, J. Šandera: Phys. Rev. B 67 (2003) 035116.
[125] D. Legut, M. Friák, M. Šob, in Proceedings of the International Conference Juniormat'01, Institute of Materials Engineering, Brno University of Technology, Brno, 2001, pp. 198–201.
[126] N. Nagasako, M. Jahnatek, R. Asahi, J. Hafner: Phys. Rev. B 81 (2010) 094108.
[127] S. Ogata, J. Li: J. App. Phys. 106 (2009) 113534.
[128] M. Jahnatek, J. Hafner, M. Krajci: Phys. Rev. B 79 (2009) 224103.
[129] J. M. Zhang, Y. Yang, K. W. Xu, V. Ji: Comp. Mat. Sci. 43 (2008) 917.
[130] J. M. Zhang, Y. Yang, K. W. Xu, V. Ji: Canadian J. Phys. 86 (2008) 935.
[131] H. Wang, M. Li: J. Phys. Cond. Mat. 22 (2010) 295405.
[132] Y. L. Liu, Y. Zhang, R. J. Hong, G. H. Lu: Chinese Phys. B 18 (2009) 1923.
[133] Y. L. Liu, H. B. Zhou, Y. Zhang, S. Jin, G. H. Lu: Nuc. Instrum. Meth. Phys. Res. Sec. B 18 (2009) 3282.
[134] J. Z. Wang, J. M. Zhang, K. W. Xu: Crys. Res. Tech. 44 (2009) 184.
[135] J. Bhattacharya, A. Van der Ven: Acta Mater. 56 (2008) 4226.
[136] M. J. Mehl, D. Finkenstadt:, Phys. Rev. B 77 (2008) 052102.
[137] H. Djohari, F. Milstein, D. Maroudas: App. Phys. Let. 90 (2007) 161910.
[138] Y. L. Liu, Y. Zhang, H. B. Zhou, G. H. Lu, M. Kohyama: J. Phys. Cond. Mat. 20 (2008) 335216.
[139] D. Holec, F. Rovere, P. H. Mayrhofer, P. B. Barna: Script. Mat. 62 (2010) 349.
[140] M. Jahnatek, M. Krajci, J. Hafner: Phys. Rev. B 76 (2007) 014110.
[141] R. F. Zhang, S. H. Sheng, S. Veprek: App. Phys. Let. 91 (2007) 031906.
[142] X. Cui, J. T. Wang, X. X. Liang, G. Z. Zhao: Chinese Phys. Lett. 27 (2010) 027101.
[143] H. B. Zhou, Y. Zhang, Y. L. Liu, M. Kohyama, P. G. Yin, G. H. Lu: J. Phys. Cond. Mat. 21 (2009) 175407.
[144] G. L. Xu, D. L. Zhang, Y. Z. Xia, X. F. Liu, Y. F. Liu, X. Z. Zhang: Chinese Phys. Let. 26 (2009) 046302.
[145] D. Legut, M. Šob: Materials Structure and Micromechanics of Fracture V, Book series: Mat-erials Science Forum 567–568 (2008) 77–80.
[146] R. F. Zhang, D. Legut, R. Niewa, A. S. Argon, S. Veprek: Phys. Rev B 82 (2010) 104104.
[147] F. Liu, P. M. Ming, J. Li: Phys. Rev. B 76 (2007) 064120.
[148] T. Shimada, Y. Ishii, T. Kitamura: Phys. Rev. B 81 (2010) 134420.
[149] S. Ogata, Y. Umeno, M. Kohyama: Model. Sim. Mat. Sci. Eng. 17 (2009) 013001.
[150] C. J. Pickard, R. J. Needs: J. Phys. Cond. Mat. 21 (2009) 45220.
[151] H. T. Li, J. M. Zhang, K. W. Xu: Mat. Sci. Eng. A 485 (2008) 627.
[152] R. Janisch, N. Ahmed, A. Hartmaier: Phys. Rev. B 81 (2010) 184108.
[153] Z. Sun, D. Music, R. Ahuja, S. Li, J. M. Schneider: Phys. Rev. B 70 (2004) 092102.
[154] D. Music, Z. Sun, A. A. Voevodin, J. M. Schneider: Solid State Commun. 139 (2006) 139.
[155] J. M. Schneider, D. P. Sigumonrong, D. Music, C. Walter, J. Emmerlich, R. Iskandar, J. Mayer: Scripta Mater. 57 (2007) 1137.
[156] D. Raabe, B. Sander, M. Friák, D. Ma, J. Neugebauer: Acta Mater. 55 (2007) 4475.
[157] S. F. Pugh: Philos. Mag. 45 (1954) 823.
[158] I. Steinbach: Modelling Simul. Mater. Sci. Eng. 17 (2009) 073001.
[159] R. E. Miller, E. B. Tadmor: Modelling Simul. Mater. Sci. Eng. 17 (2009) 053001.
[160] T. Belytschko, R. Gracie, G. Ventura: Modelling Simul. Mater. Sci. Eng. 17 (2009) 043001.
[161] S. Narasimhan, S. de Gironcoli: Phys. Rev. B 65 (2002) 064302.
[162] J. Xie, S. de Gironcoli, S. Baroni, M. Scheffler: Phys. Rev. B 59 (1999) 965.
[163] A. Debernardi, M. Alouani, H. Dreyss: Phys. Rev. B 63 (2001) 064305.
[164] V. L. Moruzzi, J. F. Janak, K. Schwarz: Phys. Rev. B 37 (1988) 790.
[165] B. Grabowski, T. Hickel, J. Neugebauer: Phys. Rev. B 76 (2007) 024309.
[166] W. Nolting, A. Vega, T. Fauster: Z. Phys. B: Condens. Matter 96 (1995) 357.
[167] J. Kübler: J. Phys.: Condens. Matter 18 (2006) 9795.
[168] J. Kübler, G. H. Fecher, C. Felser: Phys. Rev. B 76 (2007) 024414.
[169] S. V. Halilov, A. Y. Perlov, P. M. Oppeneer, H. Eschrig: Europhys. Lett. 39 (1997) 91.
[170] N. M. Rosengaard, B. Johansson:, Phys. Rev. B 55 (1997) 14975.
[171] J. Rusz, L. Bergqvist, J. Kudrnovský, I. Turek: Phys. Rev. B 73 (2006) 214412.
[172] M. Ležaić, P. Mavropoulos, S. Blügel: Appl. Phys. Lett. 90 (2007) 082504.
[173] A. V. Ruban, S. Khmelevskyi, P. Mohn, B. Johansson: Phys. Rev. B 75 (2007) 054402.
[174] G. Y. Gao, K. L. Yao, E. Şaşioğlu, L. M. Sandratskii, Z. L. Liu, J. L. Jiang: Phys. Rev. B 75 (2007) 174442.
[175] M. Pajda, J. Kudrnovsky, I. Turek, V. Drchal, P. Bruno: Phys. Rev. B 64 (2001) 174402.
[176] F. Körmann, A. Dick, B. Grabowski, B. Hallstedt, T. Hickel, J. Neugebauer: Phys. Rev. B 78 (2008) 033102.
[177] F. Körmann, A. Dick, T. Hickel, J. Neugebauer: Phys. Rev. B 81 (2010) 134425.
[178] B. Hallstedt, D. Djurovic, J. von Appen, R. Dronskowski, A. Dick, F. Körmann, T. Hickel, J. Neugebauer: CALPHAD 34 (2010) 129.

